RSC Advances

PAPER

View Article Online
View Journal | View Issue

Cite this: *RSC Adv.*, 2021, **11**, 35361

Oxygen vacancies generated by Sn-doped ZrO_2 promoting the synthesis of dimethyl carbonate from methanol and CO_2

Shixian Song,[a] Jinyi Wei,[a] Xuan He,[a] Guangfu Yan,[a] Mengyan Jiao,[a] Wei Zeng,[a] Fangfang Dai[ab] and Midong Shi *[a]

Received 21st September 2021
Accepted 26th October 2021

DOI: 10.1039/d1ra07060f

rsc.li/rsc-advances

Oxygen vacancy sites on a catalyst surface have been extensively studied and been proved to promote the adsorption and activation of carbon dioxide. We use Sn-doped ZrO_2 to prepare a Zr/Sn catalyst rich in oxygen vacancies (OVs) by co-precipitation. The yield of dimethyl carbonate is 5 times that of ZrO_2. Compared with the original ZrO_2, Zr/Sn exhibits a higher specific surface area, number of acid–base sites and a lower band gap, which improves the conductivity of electrons and creates more surface. The number of reaction sites greatly enhances the adsorption and activation capacity of CO_2 molecules on the catalyst surface. *In situ* infrared spectroscopy shows that CO_2 adsorbs on oxygen vacancies to form monomethyl carbonate, and participates in the reaction as an intermediate species. This work provides new clues for the preparation of ZrO_2-based catalysts rich in oxygen vacancies to directly catalyze the synthesis of dimethyl carbonate from methanol and CO_2.

1. Introduction

Dimethyl carbonate (DMC) is considered to be one of the important green chemical raw materials in the 21st century because of its multiple active functional groups and low toxicity.[1] Dimethyl carbonate has high oxygen content (53%) and high octane number (105), and is considered an excellent fuel additive, which can be used to reduce CO, NO_x, and SO_x emissions.[2,3] The methyl, methoxy and carboxyl groups contained in DMC can replace the carboxylation and methylation reactions of phosgene and dimethyl sulfate.[4] Furthermore, DMC has broad application prospects in organic synthesis, pesticides, medicine, spices, additives, *etc.*[5–7] It can be directly synthesized from CO_2 and methanol as raw materials. This method is considered to be a green, environmentally friendly, and very promising synthesis method.

Metal oxides have a wide range of applications in the fields of chemistry, physics, and materials science. Their redox properties and acid–base sites are very important for absorption and catalytic applications. In the literature, CeO_2, ZrO_2, SnO_2, TiO_2, V_2O_5, Y_2O_3, Ga_2O_3 and other single metal oxides and their composite oxides have been used to catalyze the direct synthesis of DMC from CO_2 and methanol.[8–12] However, because CO_2 has the characteristics of thermodynamic stability and chemical inertness, the route of direct synthesis of DMC still faces limiting factors such as low yield and kinetics/thermodynamics. It is well known that acidity and basicity of the catalytic sites of CO_2 adsorption are the key factors that determine the efficiency of CO_2 activation.

Oxygen vacancies (OVs) on the surface of the catalyst can not only promote the adsorption and activation of CO_2, but also serve as active sites for CO_2 conversion in the methanation of CO_2.[13,14] Oxygen vacancies affect the effect of carbon dioxide catalytic reaction by promoting electron transfer. It has been shown that OVs enhance the catalytic performance of the catalyst by widening the valence band (VB) and narrowing the band gap, and inhibiting photo-induced electron–hole recombination.[15,16]

Crystal form of zirconia catalyst has a great influence on the acidity and basicity of the catalyst surface and the surface oxygen vacancies. Oxygen vacancies are ubiquitous in metal oxides and have obvious effects on the physical and chemical properties of materials.[17,18] Bell *et al.*[19] studied the formation rate of methoxy and methyl carbonate on the tetragonal and monoclinic phases of zirconia, and found that zirconia with a tetragonal crystal phase had a higher density and strength of acid–base sites point, making the formation of methyl groups easier on the tetragonal phase. Methoxy and methyl carbonate are important intermediate species in the direct synthesis of DMC. Compared with pure zirconia, doping other metal ions into zirconia will change the oxygen vacancy concentration and acidity and alkalinity of the catalyst surface.[20–22] Tomishige *et al.*[23] found that the catalytic activity of ZrO_2 catalyst for the synthesis of DMC is significantly improved compared with pure ZrO_2, which is related to the oxygen vacancies generated by the introduction of Ce^{4+}. However, the internal effect of OVs on the

[a]College of Chemistry and Environmental Science, Hunan Province Key Laboratory of Rare and Precious Metal Compounds, Xiangnan University, Chenzhou 423000, Hunan, China. E-mail: mdshi032825@xnu.edu.cn

[b]Shaanxi Key Laboratory of Chemical Additives for Industry, Shaanxi University of Science and Technology, Xi'an 710021, China

catalytic reaction is still elusive, which hinders the rational design of catalyst defects.

Herein, zirconia catalysts with different Sn content were prepared by co-precipitation and their activity in the direct synthesis of dimethyl carbonic from methanol and carbon dioxide was explored. TEM, XRD, N_2 adsorption, UV-Vis spectroscopy, Raman spectroscopy, CO_2/NH_3-TPD, XPS technology and *in situ* FTIR techniques were employed to identify the structure and composition of the prepared catalysts. The importance of oxygen vacancy for the synthesis of dimethyl carbonate has been studied in detail.

2. Experimental

2.1. Materials

Crystallization of stannic chloride ($SnCl_4 \cdot 5H_2O$, AR) was obtained from Guangdong WengJiang Chemical Reagent Co, Ltd (Guangdong, China), Zirconium nitrate ($Zr(NO_3)_4 \cdot 5H_2O$, AR) was purchased from RON Reagent (Shanghai, China), ammonia ($NH_3 \cdot H_2O$, AR) was obtained from Pingxiang White Lion Chemical Reagent Co, Ltd (Jiangxi, China). All the above have not been a reagent reaction under the further purification.

2.2. Catalyst preparation

ZrO_2/SnO_2 was synthesized by co-precipitation method. As shown in Fig. 1, the mixture of zirconium nitrate and tin tetrachloride with molar ratios of 1 : 1, 1.5 : 1, 2.5 : 1, 4 : 1 and 5.5 : 1 was placed in 250 ml of deionized water, and stirred until completely dissolved. After dissolving, $NH_3 \cdot H_2O$ was added into the above solution to pH = 9–10 and stirring was continued for 1 hour. Then the stirring was stopped, the product was aged and left standing for 12 hours at room temperature. When the aging product was filtered, it was washed with deionized water to neutrality until pH = 7, and washed 3–4 times with ethanol. The product after suction filtration was dried at 100 °C for 12 hours, and then calcined in a muffle furnace at 400 °C for 5 hours to obtain Zr_n/Sn, where is the molar ratio of Zr to Sn, and the molar ratio of Zr to Sn is controlled at 1 to 5.5.

2.3. Catalyst characterization

The morphology of the catalyst powder was characterized by Tecnai G2F20 transmission electron microscope with the acceleration voltage of 200 kV. The analytical sample was dispersed in ethanol in the form of catalyst powder and then deposited on the carbon film on the copper grid.

The phase structure of the catalysts was characterized by XRD (D/max-Ultima IV) using a Cu target Kα-ray (40 kV and 30 mA) as the X-ray source. The scanning range (2θ) was from 10° to 80° with a scanning speed of 8° min^{-1} and a step function of 0.02.

The specific surface area and pore structure of the catalyst were measured by the Nitrogen adsorption method using the Micromeritics TriStar II Specific Surface Analyzer at the temperature of liquid nitrogen. Before the test, the sample was degassed at a temperature of 180 °C for 6 hours, and the isothermal desorption branch analysis was performed through the Barrett–Joyner–Halenda (BJH) model to calculate the pore volume and pore size distribution, and use the Brunauer–Emmett–Teller (BET) method to estimate the catalyst specific surface area.

The model of the Raman spectrometer used was Horiba Scientific LabRAM HR Evolution installed an Ar laser with a wavelength of 514.5 nm and an output power of 4 mW. The UV-Vis spectrum of the catalyst sample was obtained by Shimadzu UV-2600 UV spectrophotometer.

X-ray photoelectron spectroscopy (XPS) was performed on Thermo Scientific K-Alpha using a 300 W AlK X-ray source, a constant residence time of 100 ms, and a transfer energy of 40 eV. The binding energy refers to the C1s hydrocarbon peak at 284.8 eV.

Temperature programmed desorption (TPD) was performed on the automatic chemical adsorption analyzer PCA-1200. The 0.1 g sample was pretreated at 180 °C for 1 h under He. Then, CO_2/NH_3 was adsorbed at 25 °C for 60 minutes. After the adsorption was completed, the sample was purified with He for 1 hour to remove physically adsorbed CO_2/NH_3. At a constant flow rate of He, the test was performed by heating from 50 °C to 600 °C at a heating rate of 10 °C min^{-1}. Use TCD to continuously detect the CO_2/NH_3 concentration in the exhaust gas.

The *in situ* infrared spectroscopy experiment was performed on a Thermo Scientific Nicolet IS50 infrared spectrometer with a resolution of 8 cm^{-1} and 128 scans accumulated. Add 20 mg of catalyst powder to the diffuse reflection cell, heat it for 2 h under a He atmosphere at 180 °C, and measure the background spectrum after it is cooled to room temperature. The flow rates of He and CO_2 are 30 ml min^{-1} and 20 ml min^{-1}, respectively. DMC and methanol are injected into the infrared cell through

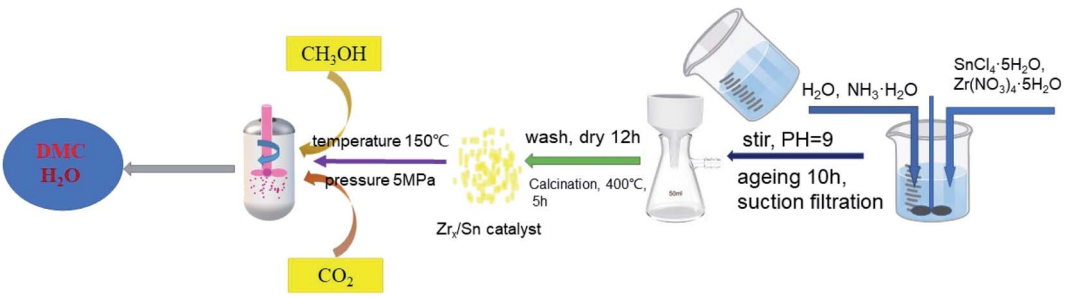

Fig. 1 Schematic diagram of the synthesis of Sn-doped ZrO_2 catalyst and the direct synthesis of dimethyl carbonate from methanol and carbon dioxide.

He gas flow, and the flow rates are 10 ml min^{-1} and 20 ml min^{-1}. When CO_2, methanol and DMC are introduced into the reaction unit, the temperature is maintained at 25 °C.

2.4. Catalyst performance evaluation

The DMC synthesis was carried out in a micro-reactor with continuous stirring function, and the inner tank volume of the reactor is 100 ml. 0.8 g of catalyst and 40 ml of methanol were put into the autoclave reactor. Before the reaction started, the reactor was cleaned with carbon dioxide several times to exhaust air. Then, the pressure of carbon dioxide in the reactor was pressurized to 5 MPa at room temperature, and the reaction temperature was increased to 150 °C. After 15 h of reaction, the reaction material was cooled to room temperature, and then the reaction solution was obtained by filtration. *N*,*N*-Dimethylformamide (DMF) was used as an internal standard substance and added to the mixture, and the product was analyzed with a gas chromatography FID detector (Zhong Kepu GC-2020). The chromatographic column type is OV-1701, 30 m × 0.32 mm × 0.5 μm. The N_2 flow rate was 30 ml min^{-1}. The sample volume was 0.2 μl per injection. The column temperature was initially 80 °C, then increased to 120 °C at a rate of 25 °C min^{-1} and held for 2 min. In this work, the yield of DMC was calculated according to the following formula:

$$\text{DMC yield} = \frac{n_{\text{DMC}}\ (\text{mmol})}{m_{\text{catalyst}}\ (\text{g})}$$

3. Results and discussion

3.1. Transmission electron microscope image of the catalysts

The TEM and HRTEM analysis were performed to explore the morphology of the prepared ZrO_2, Zr_n/Sn solid solution and pure SnO_2 (Fig. 2). All solid solutions show different degrees of agglomeration. Compared with other samples, the $Zr_{2.5}Sn$ catalyst has the largest agglomeration degree, which is not conducive to the dispersion of active sites. The particle diameters of the catalysts were related to the variation of Sn doping. Compared with ZrO_2, the diameters of Zr_1/Sn and $Zr_{1.5}$/Sn catalyst particles increased to 13.5 nm and 11.4 nm, respectively. However, as the Zr content further increases, the diameter of the catalyst particles gradually decreases.

HRTEM image can determine the crystallization characteristics of the Zr_n/Sn catalysts. The lattice fringes of 0.314 nm, 0.261 nm and 0.362 nm can be respectively referred to as the (−111), (002) and (011) planes of monoclinic ZrO_2 [PDF 86-1450], while the lattice fringes of 0.284 nm and 0.171 nm are due to (002) and (103) planes of the orthogonal $ZrSnO_4$ [PDF 48-0889]. In the SnO_2 low-magnification TEM image, the existence of particles in the dispersed state is clearly observed. The lattice fringe data of 0.331, 0.261 and 0.160 nm obtained by calculating HRTEM images confirmed the existence of (110), (101) and (220) planes of SnO_2 [PDF 41-1445], respectively.

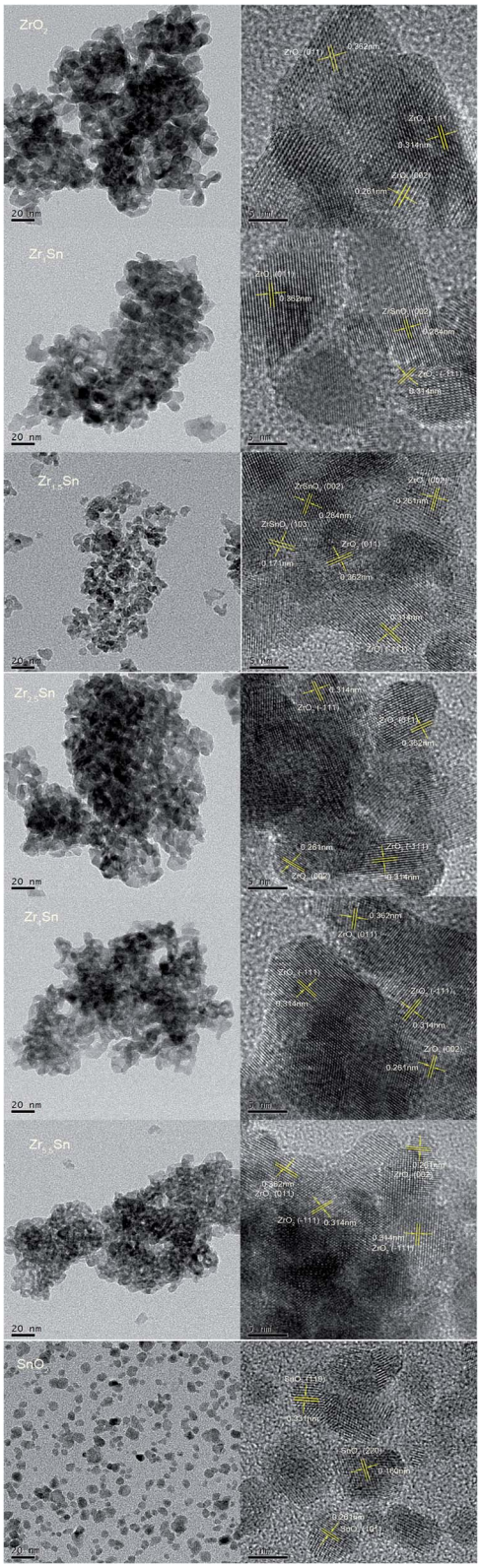

Fig. 2 TEM images of ZrO_2, Zr_n/Sn, and pure SnO_2.

3.2. XRD analysis

Fig. 3 gives the XRD patterns of Zr_n/Sn catalyst. The addition of SnO_2 makes the diffraction peaks sharper and the crystallinity of the material is higher. The diffraction peaks of the Zr_n/Sn (*n*

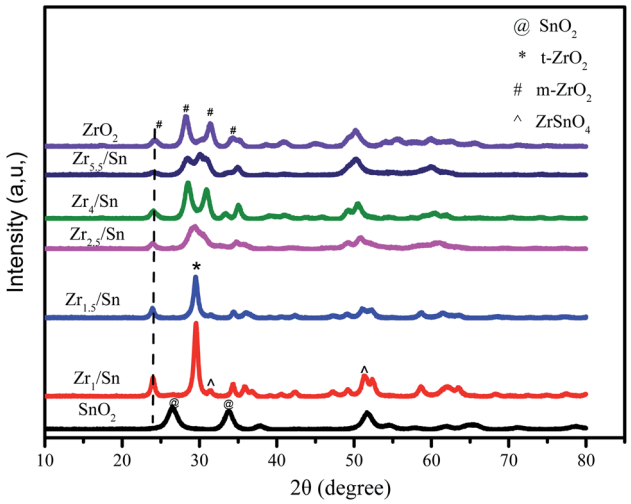

Fig. 3 XRD patterns of Zr_n/Sn catalyst.

= 1, 1.5, 2.5, 4, 5.5) catalysts move to a higher 2θ angle, indicating that Sn has been successfully inserted into the lattice structure of zirconium. The diffraction peaks at 2θ = 24.1°, 28.3°, 31.5° and 50.3° are considered to be (011), (−111), (111), (002) of monoclinic ZrO_2 [PDF 86-1450] crystal planes, 26.5° and 33.8° to be (110) and (101) crystal planes of tetragonal SnO_2 [PDF 41-1445]. Since the ionic radius of Zr^{4+} (0.79 Å) is larger than that of Sn^{4+} (0.68 Å), the substitution of Sn^{4+} ions will cause the shrinkage of ZrO_2 lattice, resulting in a decrease in the lattice parameters. The formation of solid solution is accompanied by the shrinkage of interplanar spacing, which drops from 3.71 Å to 3.64 Å. The Scherrer equation was used to calculate the average grain size of ZrO_2, Zr_1/Sn, $Zr_{1.5}$/Sn, $Zr_{2.5}$/Sn, Zr_4/Sn, $Zr_{5.5}$/Sn, and SnO_2 from the XRD results to be 91 Å, 127 Å, 110 Å, 90 Å, 87 Å, 79 Å and 56 Å, respectively (Table 1). Compared with zirconia, the grain sizes of $Zr_{2.5}$/Sn, Zr_4/Sn, and $Zr_{5.5}$/Sn are all smaller. The larger grain size of $Zr_{1.5}$/Sn and $Zr_{2.5}$/Sn may be due to the larger grain size of $ZrSnO_4$ produced during the crystallization process than tetragonal ZrO_2 and tetragonal SnO_2.[24]

According to reports by Štefanić *et al.*,[25] metastable $ZrSnO_4$ will only appear in calcination systems at 1000 °C or higher. However, according to our research, in Zr_1/Sn and $Zr_{1.5}$/Sn, 2θ = 31.5°, 51.2° show the (002) and (103) crystal plane growth of orthogonal $ZrSnO_4$ [PDF 48-0889].[26] The formation of $ZrSnO_4$ is due to the solubility of Sn^{4+} ions in the ZrO_2 lattice obtained upon crystallization. However, it is not ruled out that other Zr_n/Sn samples also contain a small amount of $ZrSnO_4$. This is because the diffraction peaks of $ZrSnO_4$ and that of t-ZrO_2 and m-ZrO_2 overlap significantly. With the increase of zirconia content, the diffraction peak intensity of SnO_2 gradually weakened, which may be caused by the excessive dispersion of SnO_2 in the ZrO_2 matrix. At the same time, the (111) crystal plane of tetragonal ZrO_2 [PDF 88-0287] appeared at 2θ = 29.6°.

In our research, it was observed that pure zirconia particles obtained a mixed tetragonal phase and monoclinic phase at an annealing temperature of 400 °C. The presence of tin makes the samples have stable tetragonal ZrO_2 (t-ZrO_2) crystal form. These crystalline products may be the result of the surface interaction of ZrO_2–SnO_2, similarly as in the ZrO_2/SO_4^{2-} system that prevents the diffusion of oxygen from the atmosphere into the ZrO_2 lattice and triggers the t-ZrO_2 to m-ZrO_2 transition.[27] The surface interaction seems to be an important factor for stabilizing the t-ZrO_2 phase in the crystalline product of the ZrO_2–SnO_2 system. Therefore, calcination in air leaves enough SnO_2 on the surface to delay the phase transition from t-ZrO_2 to m-ZrO_2 in the ZrO_2–SnO_2 system.[24]

3.3. Raman spectra of the catalyst

The Raman spectrum in Fig. 4 further illustrates the formation of Zr–Sn solid solution. The peaks of ZrO_2 particles at 179, 190, 477, 560, 634 cm^{-1} and 223, 333, 346, 537, 616 cm^{-1} respectively correspond to the A_g and B_g vibration modes of monoclinic ZrO_2 respectively.[28] In addition, the weak peak intensity at 266 cm^{-1}, 270 cm^{-1} and 307 cm^{-1} are attributed to the E_g and B_{1g} vibration modes of the tetragonal ZrO_2, respectively.[29] It is also observed that there is 382 cm^{-1} belonging to cubic ZrO_2, which is not found in the XRD pattern. The presence of cubic zirconia indicates that there is a transition from t-ZrO_2 to m-ZrO_2, which leads to the appearance of the unstable intermediate product c-ZrO_2.[30] Interestingly, by inserting Sn in the ZrO_2 lattice, it was found that with the decrease of Zr content, the Raman peak at 179 cm^{-1} has a different degree of blue shift (from 179 cm^{-1} to 176, 177, 177, 175, and 175 cm^{-1}, respectively), while the Raman peak at 190 cm^{-1} has different degrees of red shift (increasing

Table 1 Catalyst lattice spacing, average grain size, BET specific surface area and pore volume

Catalysts	2θ	Interplanar spacing[a] (Å)	Lattice parameter[b]			Average crystallite size[c] (Å)	S_{BET} ($m^2\ g^{-1}$)	V_{pore} ($cm^3\ g^{-1}$)
			a	*b*	*c*			
ZrO_2	24.07	3.71	5.18	5.21	5.35	93	80.07	0.147
Zr_1/Sn	23.92	3.64	4.95	5.20	5.73	127	56.91	0.134
$Zr_{1.5}$/Sn	23.93	3.65	4.91	5.19	5.71	110	87.81	0.133
$Zr_{2.5}$/Sn	23.96	3.67	5.17	5.19	5.34	89	84.12	0.129
Zr_4/Sn	24.01	3.68	5.16	5.17	5.31	84	103.07	0.121
$Zr_{5.5}$/Sn	24.03	3.70	5.15	5.14	5.30	79	126.03	0.109
SnO_2	26.58	3.35	4.73	4.71	3.19	56	—	—

[a] Calculated by (110) plane from XRD. [b] Calculated for Zr_1/Sn and $Zr_{1.5}$/Sn catalysts by tetragonal ZrO_2, for ZrO_2, $Zr_{2.5}$/Sn, Zr_4/Sn and $Zr_{5.5}$/Sn by monoclinic, for SnO_2 by tetragonal. [c] Estimated from XRD by Debye–Scherrer's equation.

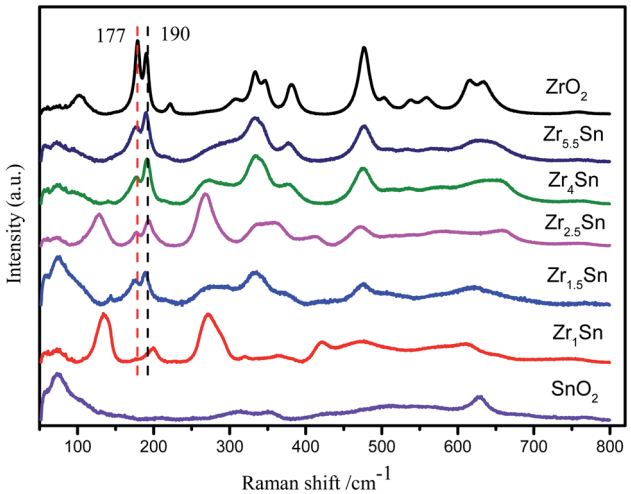

Fig. 4 Raman spectra of ZrO_2, Zr_n/Sn and SnO_2 catalysts.

from 190 cm^{-1} to 191, 191, 193, 191, 200 cm^{-1}, respectively). This is attributed to the substitution of Sn which leads to local disordered changes and defects, which may lead to lattice distortion and reduction of lattice spatial symmetry.[31] The ratio of 190 cm^{-1} peaks with faster intensity change to 177 cm^{-1} peaks with slower intensity change is selected to reflect the degree of material defects. As the amount of Sn doping increases, the strength of the I_{190}/I_{177} ratio gradually increases. It shows that the defect content in the catalyst increases with the decrease of Zr content (Table 2). This is highly consistent with the above XRD results. The Raman peak at 75 cm^{-1} in the Raman spectrum corresponds to SnO_2, and the Raman peak at 190 cm^{-1} corresponds to ZrO_2, and the two Raman peaks are less interfered. The relative intensity of ZrO_2 and SnO_2 in the material can be reflected by the change in the relative intensity of the absorption peaks. The main reason for the deviation of the data of Zr_4/Sn and $Zr_{5.5}$/Sn is that the relative content of ZrO_2 in the sample is too large, and the Raman peak at 75 cm^{-1} overlaps with the weak Raman peak of SnO_2, which leads to inaccurate calculation of the relative content.

Since the Raman shift of Sn is not observed in Zr_n/Sn, it indicates that ZrO_2 and SnO_2 form a solid solution. For pure SnO_2, the vibration modes at 73 cm^{-1}, 633 cm^{-1} and 770 cm^{-1} are attributed to the B_{1g}, A_{1g} and B_{2g} vibration modes, respectively, which belong to the natural mode of tetragonal rutile.[32] The A_{1g} and B_{2g} modes may be related to the stretching vibration of the Sn–O bond, while B_{1g} is more related to the oxygen atom rotating around the *C* axis.

3.4. UV-Visible spectrum

Compared with pure ZrO_2, the absorption edges of other samples have different degrees of blue shift, and the absorption intensity is enhanced. The existence of oxygen vacancies in Zr_n/Sn makes a new energy level formed in the band gap, so there is a new absorption peak in the range of 250 nm to 350 nm. Draw the relationship between $(\alpha h\nu)^{1/2}$ and $h\nu$ according to the information in Fig. 5, and calculate the extrapolated intercept relative to E_g, where α is the absorption coefficient and hυ is the photon energy. The E_g values of ZrO_2, Zr_1/Sn, $Zr_{1.5}$/Sn, $Zr_{2.5}$/Sn, Zr_4/Sn and $Zr_{5.5}$/Sn are 4.58, 3.32, 2.96, 2.95, 2.85 and 2.70 eV, respectively (Fig. 6).

With the increase of Sn dopant, the red shift of the interference-free region can be observed, indicating that the band gap of the Zr/Sn catalyst is significantly reduced (from 4.58 eV to 2.70 eV). This may be due to the sp-d spin-exchange interaction between the electron-carrying electron at the cation site and the local d-electron of the Zr ion or the increase in the surface area to volume ratio.[33] The first interaction lowers the bottom of the conduction band, and the second interaction increases the top of the valence band, narrowing the band gap. The introduction of impurity bands and the trapping of Zr atoms at the grain boundaries result in the formation of Zr defect states in the forbidden band.[34] As Zr doping increases, the density of Zr-induced defect states increases, leading to the observed band gap red shift or decrease.

In order to prove that the introduction of Zr defect states in the band gap region will cause the change of disorder, we introduce a concept $1/D$.[26] $1/D$ represents the average crystallite size, which is determined by the ratio of the surface area to the volume of the constituent particles of the sample. As the grain size decreases, more and more disorder is introduced into the sample. Therefore, $1/D$ can be considered as a measure of crystal disorder. Since the radius of Sn ions is smaller than that of Zr ions, as the content of Zr increases, more disorder may be introduced into the particles. Fig. 6g shows that the band gap of the Zr/Sn catalyst increases with increasing particle disorder.

The results show that Sn doping in ZrO_2 effectively reduces the band gap energy, the substitution of Zr^{4+} with Sn species facilitates the formation of Zr^{3+}ions, leading to a rise of oxygen vacancy concentration in Sn-doped ZrO_2 through distorting the lattice structure.[35,36]

Table 2 Zr_n/Sn specific peak area ratio in Raman spectrum

Catalysts	Zr_1/Sn	$Zr_{1.5}$/Sn	$Zr_{2.5}$/Sn	Zr_4/Sn	$Zr_{5.5}$/Sn
I_{190}/I_{177}	3.66	1.72	1.69	1.66	1.38
I_{190}/I_{75}	1.16	1.47	2.71	4.35	5.71

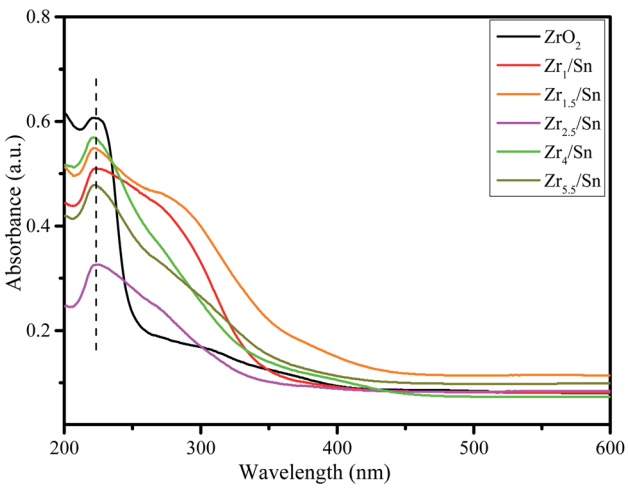

Fig. 5 UV-vis absorption spectra of ZrO_2 and Zr_n/Sn.

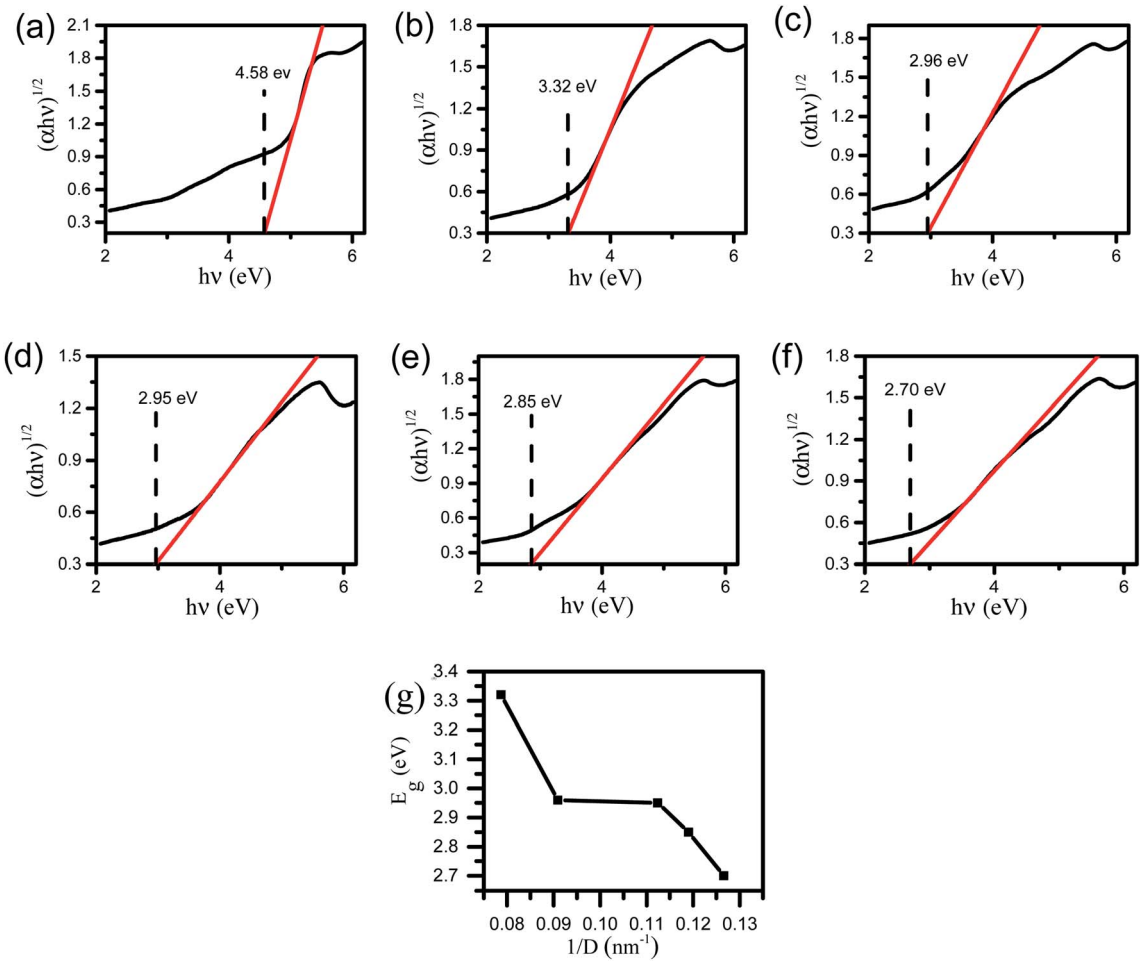

Fig. 6 The Tauc diagram derived from the ultraviolet-visible spectrum is used to estimate the optical band gap of semiconductors. (a) ZrO_2, (b) Zr_1/Sn, (c) $Zr_{1.5}$/Sn, (d) $Zr_{2.5}$/Sn, (e) Zr_4/Sn, (f) $Zr_{5.5}$/Sn; (g) the relationship between crystal grain size (1/*D*) and band gap in Zr/Sn catalyst.

3.5. Temperature programmed desorption test of catalyst

It is reported that the surface oxygen vacancies of the catalyst and the Lewis acid sites play an equally important role in CO_2 adsorption.[14] Temperature programmed desorption (TPD) can provide the information on the strength and number of acidic and basic sites on the surface of the catalyst. Therefore, we use NH_3-TPD and CO_2-TPD to study the surface properties of the catalyst (Fig. 7). The amount of CO_2 desorbed by the catalyst in Table 3 is calculated after the desorption peak is deconvolved. The desorption peaks of CO_2 appear in the range of 50–150, 200–400, 400–550 °C, which are weak adsorption sites, medium adsorption sites and strong adsorption sites, respectively. We can observe that in the range of 200–400 °C, the peak intensity shows a trend of first decreasing, then increasing and then

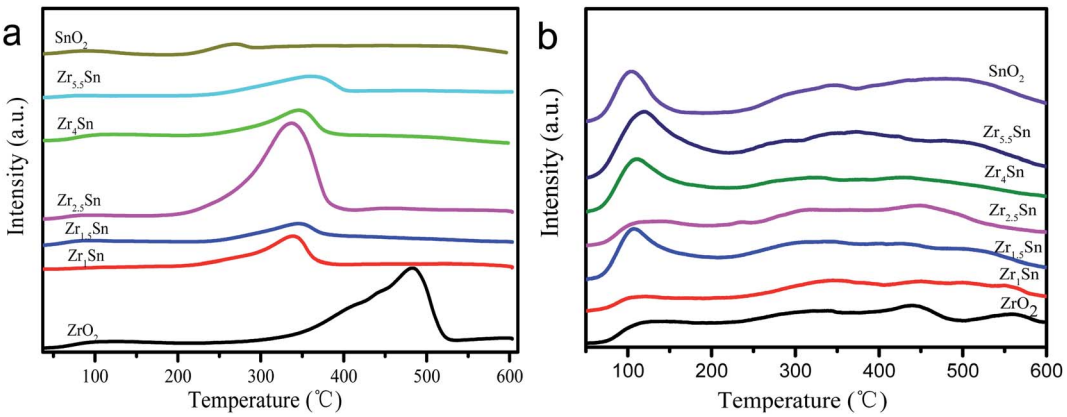

Fig. 7 TPD profiles of ZrO_2, Zr_n/Sn and SnO_2. (a) CO_2-TPD, (b) NH_3-TPD.

Table 3 Relative acidity and basicity calculated from NH_3-TPD and CO_2-TPD measurements

	Acid sites distribution of NH_3-TPD measurement data[a]				Basic sites distribution of CO_2-TPD measurement data[b]			
	Weak[c]	Moderate	Strong	Total	Weak	Moderate	Strong	Total
SnO_2	0.26	0.55	0.17	0.98	0.12	0.13	0.12	0.36
Zr_1/Sn	0.07	0.26	0.07	0.40	0.11	0.46	0.14	0.71
$Zr_{1.5}$/Sn	0.19	0.50	0.08	0.77	0.12	0.19	0.01	0.32
$Zr_{2.5}$/Sn	0.17	0.42	0.35	0.94	0.05	1.32	0.10	1.47
Zr_4/Sn	0.33	0.23	0.44	1.00	0.13	0.49	0.38	1.00
$Zr_{5.5}$/Sn	0.26	0.37	0.20	0.83	0.09	0.44	0.20	0.73
ZrO_2	0.03	0.32	0.11	0.41	0.11	0.75	0.58	1.44

[a] Set the amount of acidic sites of Zr_4/Sn as 1.00, and compare with other samples. [b] Set the amount of basicity sites of Zr_4/Sn as 1.00, and compare with other samples. [c] Weak (<200 °C), moderate (200 °C to 400 °C), strong (>400 °C).

decreasing with the decrease of Zr content. Zr_4/Sn contains the highest number of weak acid sites, which is second only to ZrO_2 and $Zr_{1.5}$/Sn in the number of neutral acid sites, and the number of strong acid sites is only lower than ZrO_2. The total amount of CO_2 adsorbed by Zr_n/Sn catalyst is lower than that of ZrO_2 (except $Zr_{2.5}$/Sn), and higher than that of SnO_2 catalyst (except $Zr_{1.5}$/Sn). The amount of CO_2 adsorbed by these catalysts shows a wave-shaped curve relative to the content of Zr and followed the order: $Zr_{2.5}$/Sn > ZrO_2 > Zr_4/Sn > $Zr_{5.5}$/Sn > Zr_1/Sn > SnO_2 > $Zr_{1.5}$/Sn. The positive or negative charge in the model structure is the reason why the mixed oxide produces acidic sites. Since the difference in electronegativity between the two transition metals (M_1–O–M_2) will lead to an imbalance of charges, new acid sites with different strengths will be generated. It can be noticed in Fig. 7a that, compared with ZrO_2, the high temperature signal (at 400–550 °C) of the Zr_n/Sn catalyst changes to a lower temperature signal (<400 °C), which clearly shows the synergistic effect between ZrO_2 and SnO_2.[37]

The results of using NH_3-TPD to study the acid properties of the catalyst surface are shown in Table 3 and Fig. 7b. It can be observed from the figure that ZrO_2, Zr_n/Sn and SnO_2 catalysts have the same type of acid sites. The desorption peaks in the range of 50–200, 200–400, 400–600 °C can be referred to as weak adsorption, medium adsorption and strong adsorption, respectively. The NH_3 adsorption capacity of these catalysts is also calculated and summarized in Table 3. Compared with other catalysts, Zr_4/Sn catalyst has the highest NH_3 adsorption capacity, indicating that Zr_4/Sn catalyst has the most acidic sites. The adsorption amount of NH_3 in all samples relative to the content of Zr shows a volcanic curve in the following the order: Zr_4/Sn > SnO_2 > $Zr_{2.5}$/Sn > $Zr_{5.5}$/Sn > $Zr_{1.5}$/Sn > ZrO_2 > Zr_1/Sn. The total acidity of Zr_n/Sn catalyst is higher than that of pure ZrO_2 catalyst (except Zr_1/Sn), demonstrating ZrO_2 and SnO_2 have a synergistic effect. At the same time, the total acidity of Zr_1/Sn catalyst is lower than that of the ZrO_2 catalyst, which may be due to the lower BET surface area (56.91 $m^2\ g^{-1}$) and pore volume of Zr_1/Sn catalyst than the pure ZrO_2 catalyst (80.07 $m^2\ g^{-1}$), resulting in a smaller number of exposed Lewis acid sites. Similar to the results of CO_2-TPD, with the increase of Zr content, the weakly acidic sites of all Zr_n/Sn catalysts first increase and then decrease, and then increase and finally decrease. It can be found that the Zr_4/Sn catalyst has the largest number of acidic sites. By doping with oxides, the acid–base properties of ZrO_2 surface will be significantly changed, accompanied by differences in performance, similar results are obtained from previous reports.[38–40]

3.6. XPS analysis of catalyst

In order to further study the chemical state of the catalyst composition and the surface oxygen vacancy concentration, we compared the X-ray photoelectron spectroscopy (XPS) of the Zr3d and O1s regions of Zr_n/Sn and pure ZrO_2. The spectrum of pure ZrO_2 can be divided into 4 peaks after deconvolution. The prominent Zr3d$_{5/2}$ peak at 182.56 eV corresponds to the Zr^{4+} of zirconia, while the intensity between Zr^{4+} (182.56 eV) and Zr^0 (178.3 eV) is attributed to $Zr^{(4-x)+}$, and no metallic zirconium is found.[41]

Table 4 The relative ratio of $Zr^{(4-x)+}$ surface concentration and surface oxygen vacancy concentration based on XPS analysis

	Zr3d (%)		O1s (%)				
Samples	$Zr^{(4-x)+}$	ZrO_2	O_L	O_V	O_C	Surface atomic ratio Zr/Sn[a] (%)	Relative peak intensity Zr/Ce[b] (%)
ZrO_2	4.28	95.72	75.50	9.50	15.00	—	—
Zr_1/Sn	7.12	92.88	77.50	18.68	3.82	1.18	1.16
$Zr_{1.5}$/Sn	25.41	74.59	70.40	20.20	9.40	1.64	1.79
$Zr_{2.5}$/Sn	31.26	68.74	67.20	23.20	9.60	2.41	2.72
Zr_4/Sn	71.12	28.88	48.41	37.6	13.83	4.44	3.87
$Zr_{5.5}$/Sn	40.58	59.42	63.90	26.30	9.80	5.55	5.82
SnO_2	—	—	52.4	26.1	21.5	—	—

[a] Determined by XPS. [b] Determined by Raman spectra. The peak intensity at 75 cm^{-1} in the Raman spectrum of pure SnO_2 is recorded as 1, and the peak intensity at 190 cm^{-1} in the Raman spectrum of pure ZrO_2 is recorded as 1. I_{75}/I_{190} reacts to the relative content change of Zr/Sn. The spectrum has been deconvolved before calculation.

Since Sn^{4+} enters the lattice of zirconia, the binding energy of Zr3d in the Zr_n/Sn catalysts (at 182.1 eV, 184.5 eV) is higher than that of zirconia. After deconvolution calculation of the Zr3d spectrum in the ZrO_2 catalyst, Zr3d can also be decomposed into 2 groups of peaks: $Zr^{(4-x)+}$ (~181.7 eV), ZrO_2 (~182.2 eV).[42,43] In Table 4, by calculating the ratio of the area of the $Zr^{(4-x)+}$ peak to the total area of the $Zr^{(4-x)+}$ and ZrO_2 peaks, the concentration ratio of $Zr^{(4-x)+}$ can be quantitatively estimated.

The percentages of $Zr^{(4-x)+}$ to the total Zr (Zr_{total}) are 4.28%, 7.12%, 25.41%, 31.26%, 71.12% and 40.58% for the ZrO_2, Zr_1/Sn, $Zr_{1.5}$/Sn, $Zr_{2.5}$/Sn, Zr_4/Sn and $Zr_{5.5}$/Sn (Table 4), respectively. The ratio of $Zr^{(4-x)+}$ to Zr_{total} decreased in the order: Zr_4/Sn > $Zr_{5.5}$/Sn > $Zr_{2.5}$/Sn > $Zr_{1.5}$/Sn > Zr_1/Sn > ZrO_2. Furthermore, the $Zr^{(4-x)+}/Zr_{total}$ ratio of Zr_x/Sn catalysts is higher than the pure ZrO_2 sample. Table 4 shows that in the Zr_n/Sn catalysts, $Zr^{(4-x)+}$ increases with the increase of the Zr content, and then decreases with the further increase of the Zr content. This reduction is believed to be caused by catalyst aggregation caused by excess zirconium.[44] The presence of $Zr^{(4-x)+}$ was confirmed to generate oxygen vacancies on the catalyst surface. Therefore, the concentration of oxygen vacancies increases as the concentration of Zr increases. Compared with other Zr_n/Sn catalysts, Zr_4/Sn catalysts have the highest concentration of oxygen vacancies because they have the highest $Zr^{(4-x)+}/Zr_{total}$.

Fig. 8b shows the O1s XPS results on Zr_n/Sn, SnO_2 and ZrO_2 catalysts. The first peak is attributed to the lattice oxygen (O_L) in the ZrO_2 lattice at ~530.1 eV. The peaks at ~531.5 and ~532.7 eV are attributed to the O component associated with the O^{2-} ions in surface oxygen vacancies (O_V) and chemisorbed oxygen species (O_C), respectively.[45,46] Interestingly, the O1s high-resolution XPS spectrum of the Zr_n/Sn catalyst (compared to pure zirconia) has a long tail, and hopes to have a higher binding energy. The O1s spectrum of Zr_n/Sn is further deconvolved into three peaks. The component at higher binding energy could be due to C–O, O^{2-} peroxides, or OH.[47,48] The results of the quantitative calculations of the oxygen vacancy concentration on the catalyst surface are shown in Table 4.

The results show that the addition of Sn significantly reduces the lattice oxygen in the catalyst. The concentration of O_V is in good agreement with the results of the $Zr^{(4-x)+}$ concentration in the Zr3d spectrum. Due to the imbalance of oxidation state between Zr^{4+} and $Zr^{(4-x)+}$ sites, oxygen vacancies are generated, resulting in an increase in the concentration of surface oxygen vacancies. Sn doping in the zirconia lattice promotes the formation of surface oxygen vacancies/defects.[49]

The XPS spectrum of Sn3d is shown in Fig. 8c. The Zr_n/Sn catalysts showed two peaks at 495.6–495.7 eV and 487.2–487.5 eV. The peak at higher binding energy belongs to $Sn3d_{3/2}$, and the peak at lower binding energy belongs to $Sn3d_{5/2}$, which may be related to the spin–orbit splitting of $Sn3d_{3/2}$ and $Sn3d_{5/2}$.[50] The binding energy of Sn3d in the Zr_n/Sn catalyst is higher than that of tin dioxide, which further confirms that Sn^{4+} enters the zirconia lattice and forms a solid solution.

3.7. DMC yield and methanol conversion rate of different catalysts

Fig. 9 shows the catalytic performance of ZrO_2, Zr_n/Sn and SnO_2 catalysts. Zr_n/Sn catalyst has higher catalytic activity than zirconium oxide and tin oxide. The DMC yield reached 1.59 mmol g^{-1} at Zr_4/Sn, and then decreased with the further

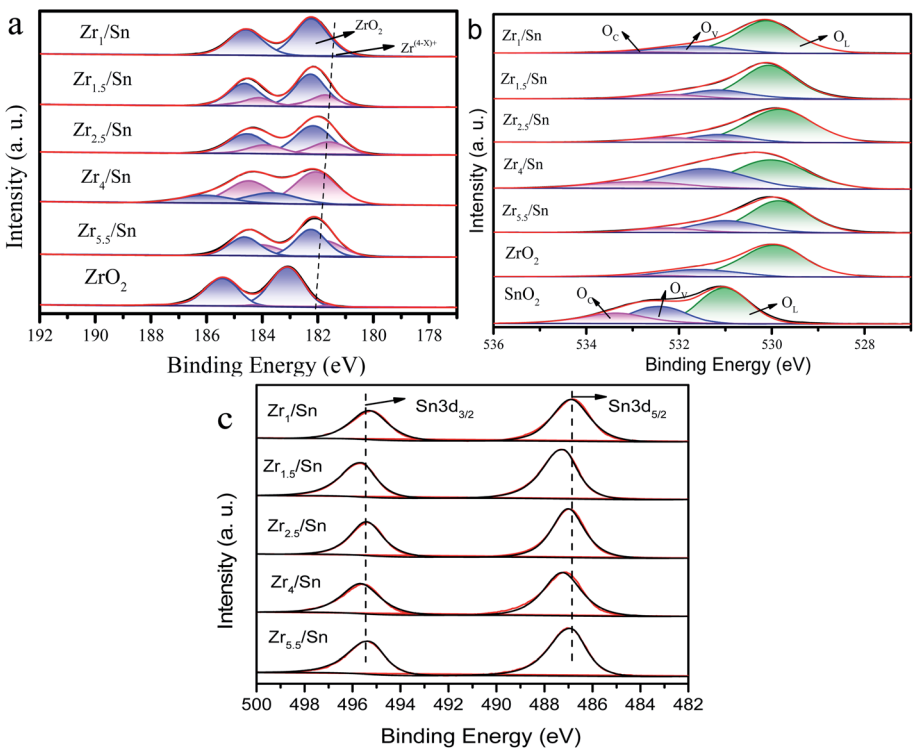

Fig. 8 (a) Zr 3d, (b) O 1s, (c) Sn 3d XPS spectra of ZrO_2, Zr_n/Sn and SnO_2.

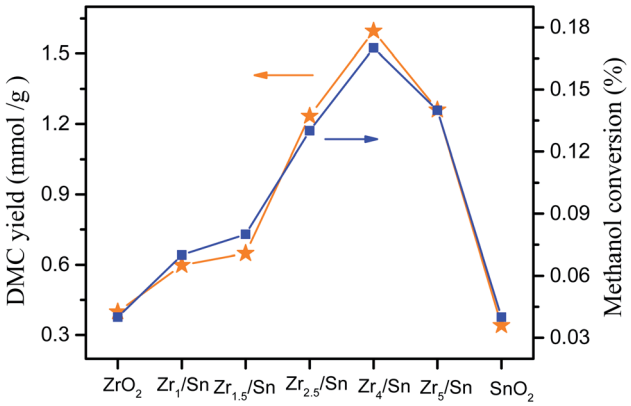

Fig. 9 Catalytic performance of different catalysts. Reaction conditions: catalyst dosage: 0.8 g; methanol: 40 ml, temperature 140 °C, pressure: 5 MPa, reaction time: 20 h. Methanol conversion = $2n_{DMC}/n_{CH3OH} \times 100\%$.

increase of the Zr/Sn ratio. According to reports, Tomishige *et al.*[23] used CeO_2–ZrO_2 to catalyze methanol and carbon dioxide to catalyze the synthesis of dimethyl carbonate, and obtained the highest DMC yield, which is 0.73 mmol (reaction temperature was 383 K, $CH_3OH : CO_2 = 192 : 200$, reaction time was 2 h, and catalyst dosage was 0.5 g). This is not the only case where lower DMC yields are also obtained. In addition, Ikeda *et al.*[8] found that the highest yield of DMC catalyzed by H_3PO_4/ZrO_2 was 0.3 mmol (reaction time was 2 h; reaction temperature was 403 K; $CH_3OH/CO_2 = 192/200$ mmol; catalyst weight was 0.5 g). This result is equally unsatisfactory, but it is what it is.

The activity of Zr_4/Sn is 3.9 times and 4.7 times that of pure zirconium dioxide and tin dioxide, respectively. The order of catalyst activity from high to low is: $Zr_4/Sn > Zr_{2.5}/Sn > Zr_{5.5}/Sn > Zr_{1.5}/Sn > Zr_1/Sn > ZrO_2 > SnO_2$, which followed the trend of the surface oxygen vacancy concentrations. It can be observed that the methanol conversion rate increases with the increase of the Zr/Sn ratio, reaching the maximum peak value of 0.17% at Zr_4/Sn, and then decreases with the further increase of the Zr/Sn ratio.

3.8. The effect of reaction time on the yield of DMC

The effect of reaction time on the catalytic synthesis of DMC with Zr_n/Sn catalysts was evaluated. The results are shown in Fig. 10a. The short reaction time (5 h) resulted in the DMC yields of Zr_1/Sn, $Zr_{1.5}/Sn$, $Zr_{2.5}/Sn$, Zr_4/Sn, $Zr_{5.5}/Sn$, SnO_2 and ZrO_2 being 0.28, 0.32, and 0.35, 0.54, 0.51, 0.22 and 0.27 mmol g^{-1}, respectively. The DMC yield at this time was at a relatively low level. The increase of the reaction time from 5 h to 25 h will significantly increase the DMC yield to 0.60, 0.65, 1.26, 1.60, 1.23, 0.34 and 0.40 mmol g^{-1}. After the reaction time exceeded 20 h, the yield of the catalyst gradually decreased, indicating that the reaction time is the best time for the maximum DMC yield at 20 h. The activity of Zr_4/Sn is the highest among all samples. This study shows that due to the accumulation of water, the optimal reaction time for the catalyst to directly synthesize DMC from methanol and carbon dioxide is 20 h.

The stability of heterogeneous catalysts has always been one of the concerns (Fig. 10b). Under the same reaction conditions as above, five reaction cycles were used to test the reusability of the catalyst in DMC synthesis. The activity of all catalysts decreased to varying degrees after five cycles of reaction. However, the catalytic activity of Zr_4/Sn is still the highest. The activities of the catalysts were reduced by 57.5, 56.7, 51.3, 31.2, 44.8, 62.9 and 59.9% after five cycle times corresponding to Zr_1/Sn, $Zr_{1.5}/Sn$, $Zr_{2.5}/Sn$, Zr_4/Sn, $Zr_{5.5}/Sn$, SnO_2, ZrO_2, respectively.

3.9. Characterization of the used catalyst

To further analyze the cause of catalyst deactivation, we compared the TEM, XRD, and XPS results of the used and fresh Zr_4/Sn catalyst (Fig. 11). According to the analysis of TEM results, the morphology of Zr_4/Sn after being recycled seven times is the same as that of fresh. However, the size of the used (~10 nm) is larger than that of the fresh (~9 nm), and the agglomeration phenomenon is more serious. The fresh and used Zr_4/Sn catalysts still show the characteristic diffraction peaks corresponding to monoclinic zirconia, which is consistent with the TEM results.

By comparing the XPS spectra of Zr3d and O1s of fresh and used Zr_4/Sn after deconvolution, it is found that the concentration of $Zr^{(4-x)+}$ and surface oxygen vacancies dropped from 71.12% and 37.6% to 11.03% and 9.1%, respectively. The reason for this reduction is that part of the O atoms used to adsorb carbon dioxide is used to fill the surface oxygen vacancies.[51] Compared to fresh, the fourth peak is attributed to adsorbed

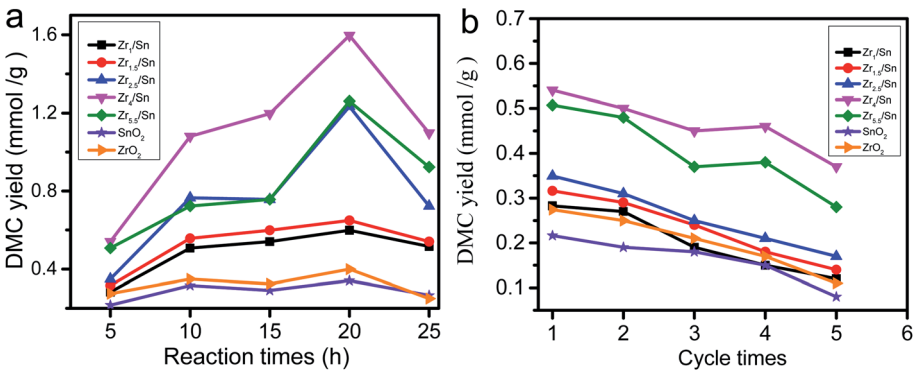

Fig. 10 The influence of reaction time on the yield of DMC. Reaction conditions: catalyst dosage: 0.8 g, methanol: 40 ml, temperature 140 °C, pressure: 5 MPa (the cycle time for one reaction is 5 hours).

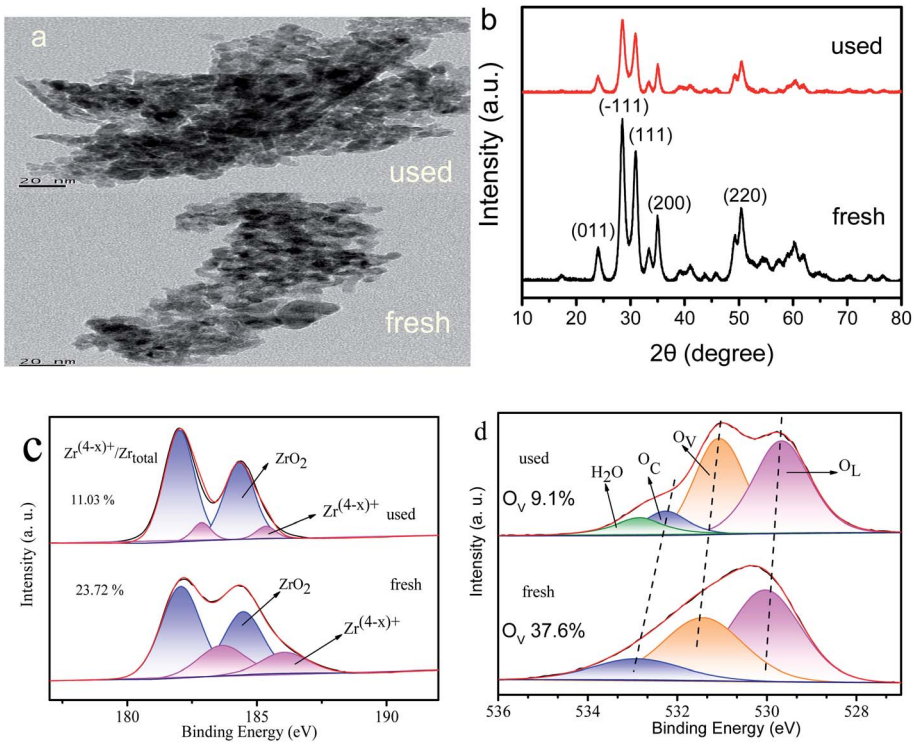

Fig. 11 TEM, XRD and XPS spectra of used and fresh catalysts. (a) TEM, (b) XRD, (c) Zr3d, (d) O1s.

water (~535.5 eV), this may be caused by too much water adsorbed in the air.[52] A large number of DFT studies and experimental studies have shown that the surface oxygen vacancies are thermodynamically unstable and highly reactive, as well as the interaction between the surface oxygen vacancies and the O atoms that adsorb carbon dioxide.[53,54]

3.10. The relationship between catalytic activity of catalyst and surface oxygen vacancy concentration and DMC yield

The surface oxygen vacancy on the catalyst surface can be used as Lewis acid sites to promote carbon dioxide adsorption.[14] Fig. 12 shows that the catalytic activity of the catalyst increases as the concentration of surface oxygen vacancies increases, indicating that surface oxygen vacancies promote the production of DMC. Oxygen vacancies can be associated with $Zr^{(4-x)+}$. The XRD, XPS and TEM images of Zr_n/Sn indicate that the increase in $Zr^{(4-x)+}$ content is due to the doping of Sn. The oxygen vacancy can interact with the non-bonded electrons in the O atom of carbon dioxide because its Lewis acid property follows the relationship of Lewis acid–base interaction.[14]

Among these catalysts, Zr_4/Sn has the greatest catalytic activity because it has the highest surface oxygen vacancy concentration. The oxygen vacancies on the surface of the oxygen defect of the metal oxide can adsorb and activate carbon dioxide, and promote the direct reaction of methanol and carbon dioxide to form DMC.[55,56] According to previous reports, the activation of carbon dioxide is achieved by filling the oxygen vacancies with free oxygen generated by the interaction at the vacancies, which is easier than on the metal surface.[57]

The methanation of carbon dioxide proves that surface oxygen vacancies can catalyze the key step that determines the rate at a lower activation temperature.[58,59] According to the results obtained in this work and previous reports, tin doping into the zirconia lattice will increase the number of active oxygen vacancies on the surface of zirconia, thereby promoting the interaction between Zr_n/Sn and carbon dioxide.[25,26,39]

3.11. *In situ* FTIR study

Fig. 13a shows the adsorption behavior of CO_2 on Zr_4/Sn. The obvious 2366 cm^{-1} linear CO_2 adsorption peak appears at room

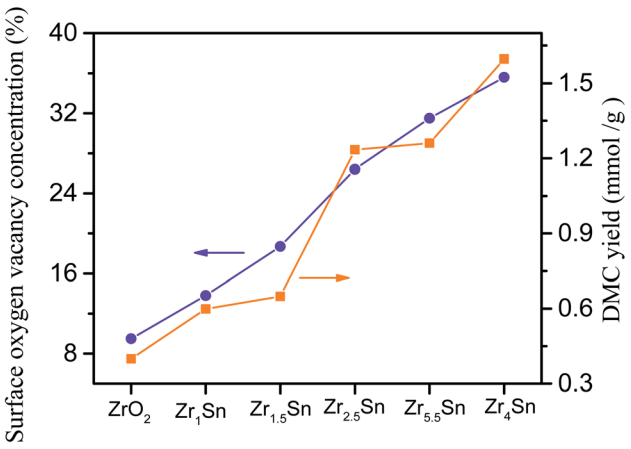

Fig. 12 The effect of surface oxygen vacancy concentration on the catalytic activity of catalyst.

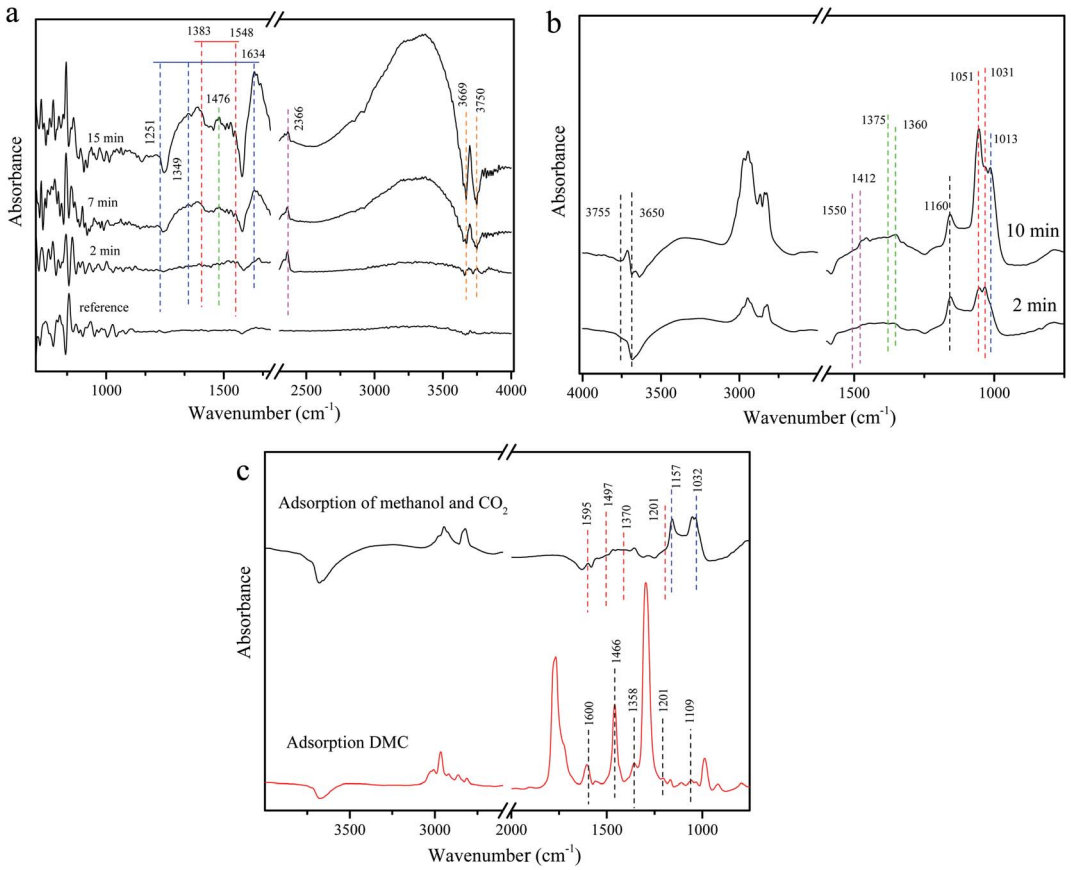

Fig. 13 DRIFTS spectra of adsorbed species on Zr_4/Sn catalyst: (a) adsorbed CO_2; (b) adsorbed methanol; (c) comparison of adsorbed DMC and CO_2 with adsorbed methanol.

temperature, which is attributed to the adsorption of CO_2 on Zr^{4+}.[60] The vibration peaks at 1634, 1349, 1251 and 1476 cm^{-1} are attributed to bicarbonate and ionic carbonate, respectively.[61] Since CO_2 reacts with the surface hydroxyl groups of ZrO_2 to generate bicarbonate, it will cause the consumption of hydroxyl groups, causing two negative peaks at 3750 and 3669 cm^{-1}.[61] At the same time, bidentate carbonate and monodentate carbonate appeared at 1548 and 1383 cm^{-1} and 1476 cm^{-1} respectively.[62]

Fig. 13b shows that when methanol is adsorbed on ZrO_2 at room temperature, they appear at 1016 cm^{-1} in addition to the apparent linear (1160 cm^{-1}) and two bridging (1052 and 1031 cm^{-1}) methoxy species.[63] Another cone-bridged methoxy species may be related to the abundant surface hydroxyl groups on the surface of ZrO_2.[63] The two negative peaks at 3755 and 3650 cm^{-1} may be caused by the reaction of surface hydroxyl groups with methanol. At the same time, the consumption of bridged hydroxyl groups is more than that of linear hydroxyl groups, which indicates that the bridged hydroxyl groups on the surface of ZrO_2 are more active than linear hydroxyl groups. Due to the effect of surface lattice oxygen, formate species appeared at 1375 and 1360 cm^{-1}, and obvious carbonate species appeared at 1550 and 1412 cm^{-1}.[64]

By exposing the catalyst to methanol for 30 minutes, flushing the infrared cell with He, and then introducing the He stream containing CO_2, the interaction between CO_2 and the adsorbed methanol material was studied. After the introduction of CO_2 in the methanol-adsorbed sample, the spectrum is very similar to the methanol adsorption on the ZrO_2 surface without pre-adsorption. In Fig. 13c, the bands appearing at 1595, 1497, 1370, and 1201 cm^{-1} can be attributed to carbonic acid monomethyl ester (m-CH_3OCOO–Zr), and the bands at 1157 and 1032 cm^{-1} are caused by methoxy substances.[19,65,66] The adsorption of DMC on the catalyst further verified the existence of monomethyl carbonate, which is an intermediate species in the direct synthesis of DMC from methanol and CO_2. Studies have shown that the high selectivity of DMC on the catalyst may be due to the rapid conversion of methoxy species to methoxy carbonate species under high carbon dioxide pressure.[67,68]

3.12. The formation mechanism of DMC on the surface of Zr_n/Sn catalyst

Fig. 14 proposes the synthesis mechanism of DMC on the surface of Zr_n/Sn catalyst. The first step of the mechanism is the adsorption and activation of carbon dioxide on the surface oxygen vacancy sites. The oxygen vacancy site is located between Zr and Sn, which is confirmed by DFT research.[69] Methanol is adsorbed and activated by the hydroxyl group at the end of Zr/Sn to form a methoxy group. The abundant terminal methoxy groups can be attributed to the high number of oxygen vacancies on the catalyst surface. In other words, the catalyst activity is restricted by the number of oxygen vacancies and the activity of adsorbed substances.

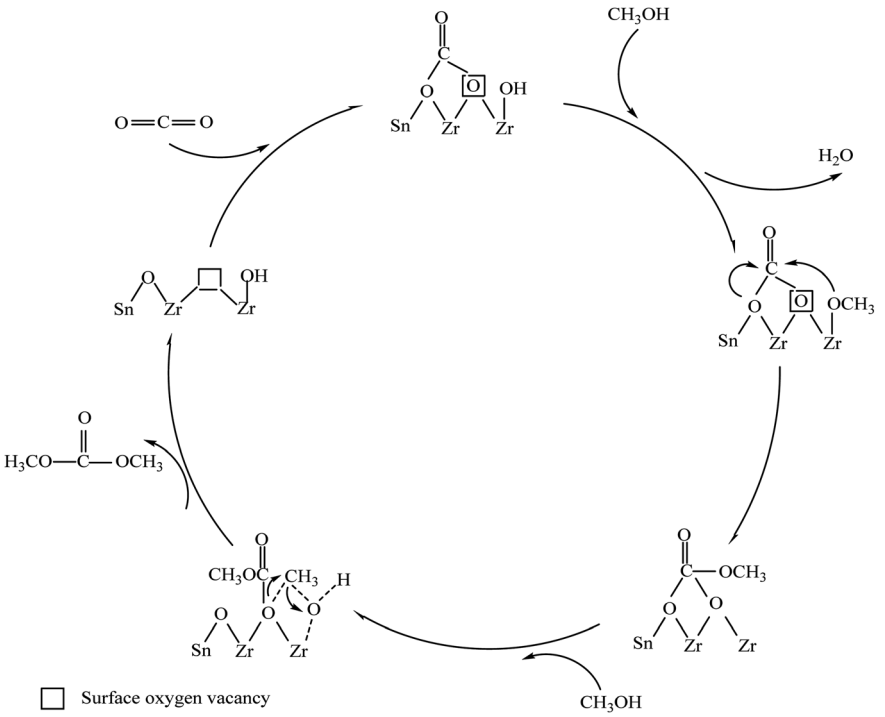

Fig. 14 Synthesis mechanism of DMC on the surface of Zr_n/Sn catalyst.

The carbon dioxide is adsorbed on the oxygen vacancies as diacid carbonate.[70] Then methanol is cleaved at adjacent acidic sites through O_M–H_4 bonds to form methyl and methoxy groups.[68] Many studies have shown that acid–base sites are critical to the activation of carbon dioxide, which will facilitate the synthesis of DMC.[71–73] The activated carbon dioxide is inserted into the oxidation bond of the methoxy species to produce monomethyl carbonate (Zr–OC(O)OCH_3), and the methyl group activated by methanol at the acidic site and methyl carbonate produce DMC.[19] Oxygen vacancy has the same effect as Lewis acid sites. The interaction with C and O in carbon dioxide and the Lewis acid–base pair ($Zr^{4+}O^{2-}$) on the catalyst surface together promote this process. The reaction of the methyl carbonate and the methyl group of the methoxy group will regenerate dimethyl carbonate and oxygen vacancy.

The results of XPS and CO_2-TPD show that doping Sn in zirconia can promote the generation of surface oxygen vacancies. Carbon dioxide will be adsorbed as bidentate carbonate on the oxygen vacancies.[74]

4. Conclusions

In this study, a series of Sn-doped zirconia catalysts were synthesized by the co-precipitation method, and the effect of tin doping on the microstructure, lattice structure, oxygen vacancy amount and the synthesis of dimethyl carbonate from methanol and carbon dioxide was studied. XRD results show that Sn doping in the ZrO_2 lattice leads to structural modification. In addition, XPS and CO_2-TPD confirmed that Sn doping can increase the generation of oxygen vacancies. The Zr_4/Sn catalyst with the highest surface oxygen vacancy concentration showed the highest catalytic activity in DMC synthesis. It was also found that the activity of DMC synthesis was related to the concentration of surface oxygen vacancies. FITR shows that the intermediate methyl carbonate and methoxy are actively involved in the synthesis of DMC. The results of this study provide reasonable guidance for the synthesis of DMC on ZrO_2 catalysts by Sn doping, and provide a technical basis for the design of new high-efficiency ZrO_2-based catalysis.

Conflicts of interest

The authors declare no competing financial interest.

Acknowledgements

This work was supported by the Hunan Provincial Natural Science Foundation of China (No. 2019JJ50566), the Projects of Scientific Research Fund of Hunan Provincial Education Department (No. 18C1017), open Fund of Hunan Provincial Key Laboratory of Xiangnan Rare-Precious Metals Compounds and Applications (No. 2019XGJSKFJJ04), the Hunan University Student Innovation and Entrepreneurship Training Program (No. S202010545040), and Scientific Research Project of Xiangnan University (No. 2018XJ21). The authors would like to thank the shiyanjia lab (www.shiyanjia.com) for support of XPS test.

References

1 N. Keller, G. Rebmann and V. Keller, *J. Mol. Catal. A: Chem.*, 2010, **317**, 1–18.

2 C. K. Westbrook, W. J. Pitz and H. J. Curran, *J. Phys. Chem. A*, 2006, **110**, 6912–6922.
3 P. Tundo and M. Selva, *Acc. Chem. Res.*, 2002, **35**, 706–716.
4 A. H. Tamboli, A. A. Chaugule and H. Kim, *Chem. Eng. J.*, 2017, **323**, 530–544.
5 R. Zevenhoven, S. Eloneva and S. Teir, *Catal. Today*, 2006, **115**, 73–79.
6 B. Schäffner, J. Holz, S. P. Verevkin and A. Börner, *ChemSusChem*, 2008, **1**, 249–253.
7 J. Bayardon, J. Holz, B. Schäffner, V. Andrushko, S. Verevkin, A. Preetz and A. Börner, *Angew. Chem., Int. Ed.*, 2007, **46**, 5971–5974.
8 K. Tomishige, T. Sakaihori, Y. Ikeda and K. Fujimoto, *Catal. Lett.*, 1999, **58**, 225–229.
9 X. L. Wu, M. Xiao, Y. Z. Meng and Y. X. Lu, *J. Mol. Catal. A: Chem.*, 2005, **238**, 158–162.
10 P. Kumar, P. With, V. C. Srivastava, R. Gläser and I. M. Mishra, *J. Alloys Compd.*, 2017, **696**, 718–726.
11 J.-C. Choi, K. Kohno, Y. Ohshima, H. Yasuda and T. Sakakura, *Catal. Commun.*, 2008, **9**, 1630–1633.
12 W. Joe, H. J. Lee, U. G. Hong, Y. S. Ahn, C. J. Song, B. J. Kwon and I. K. Song, *J. Ind. Eng. Chem.*, 2012, **18**, 1018–1022.
13 H. Over, Y. D. Kim, A. P. Seitsonen, S. Wendt, E. Lundgren, M. Schmid, P. Varga, A. Morgante and G. Ertl, *Science*, 2000, **287**, 1474.
14 C. Xin, M. Hu, K. Wang and X. Wang, *Langmuir*, 2017, **33**, 6667–6676.
15 Y. Lv, Y. Liu, Y. Zhu and Y. Zhu, *J. Mater. Chem. A*, 2014, **2**, 1174–1182.
16 R. Grabowski, J. Słoczyński, M. Śliwa, D. Mucha, R. P. Socha, M. Lachowska and J. Skrzypek, *ACS Catal.*, 2011, **1**, 266–278.
17 L. Ma, S. Chen, Z. Pei, H. Li, Z. Wang, Z. Liu, Z. Tang, J. A. Zapien and C. Zhi, *ACS Nano*, 2018, **12**, 8597–8605.
18 J. Ortiz-Medina, Z. Wang, R. Cruz-Silva, A. Morelos-Gomez, F. Wang, X. Yao, M. Terrones and M. Endo, *Adv. Mater.*, 2019, **31**, 1805717.
19 K. T. Jung and A. T. Bell, *Top. Catal.*, 2002, **20**, 97–105.
20 T. J. Keskitalo, M. K. Veringa Niemelä and A. O. I. Krause, *Langmuir*, 2007, **23**, 7612–7619.
21 H. J. Lee, W. Joe and I. K. Song, *Korean J. Chem. Eng.*, 2012, **29**, 317–322.
22 S. Pradhan, J. Saha and B. G. Mishra, *New J. Chem.*, 2017, **41**, 6616–6629.
23 K. Tomishige and K. Kunimori, *Appl. Catal., A*, 2002, **237**, 103–109.
24 V. S. Anitha, S. S. Lekshmy and K. Joy, *J. Mater. Sci.: Mater. Electron.*, 2013, **24**, 4340–4345.
25 G. Štefanić, S. Musić and M. Ivanda, *Mater. Res. Bull.*, 2008, **43**, 2855–2871.
26 V. S. Anitha, S. Sujatha Lekshmy and K. Joy, *J. Alloys Compd.*, 2016, **675**, 331–340.
27 K. Joy, S. S. Lakshmy, P. B. Nair and G. P. Daniel, *J. Alloys Compd.*, 2012, **512**, 149–155.
28 E. Fernández López, V. Sánchez Escribano, M. Panizza, M. M. Carnasciali and G. Busca, *J. Mater. Chem.*, 2001, **11**, 1891–1897.
29 H. Zhang, B. Xu, Z. Li, D. Fruchart, E. K. Hlil and L. Zhou, *Rare Met. Mater. Eng.*, 2012, **41**, 776–780.
30 Z. Wang, B. Yang, Z. Fu, W. Dong, Y. Yang and W. Liu, *Appl. Phys. A*, 2005, **81**, 691–694.
31 J. Kaur, J. Shah, R. K. Kotnala and K. C. Verma, *Ceram. Int.*, 2012, **38**, 5563–5570.
32 Y. I. Choi and Y. Sohn, *RSC Adv.*, 2014, **4**, 41292.
33 V. D. Mote, J. S. Dargad and B. N. Dole, *Nanosci. Nanoeng.*, 2013, **1**, 116–122.
34 V. I. Sokolov, A. V. Druzhinin, N. B. Gruzdev, A. Dejneka, O. Churpita, Z. Hubicka, L. Jastrabik and V. Trepakov, *Phys. Rev. B: Condens. Matter Mater. Phys.*, 2010, **81**, 153104.
35 G. Poungchan, B. Ksapabutr and M. Panapoy, *Mater. Des.*, 2016, **89**, 137–145.
36 C. Morant, J. M. Sanz and L. Galán, *Phys. Rev. B: Condens. Matter Mater. Phys.*, 1992, **45**, 1391–1398.
37 D. R. Burri, K.-M. Choi, D.-S. Han, Sujandi, N. Jiang, A. Burri and S.-E. Park, *Catal. Today*, 2008, **131**, 173–178.
38 Z. Fu, Y. Zhong, Y. Yu, L. Long, M. Xiao, D. Han, S. Wang and Y. Meng, *ACS Omega*, 2018, **3**, 198–207.
39 G.-W. Wang, H. Hattori and K. Tanabe, *Bull. Chem. Soc. Jpn.*, 1983, **56**, 2407–2410.
40 B. Liu, C. Li, G. Zhang, X. Yao, S. S. C. Chuang and Z. Li, *ACS Catal.*, 2018, **8**, 10446–10456.
41 M. A. Rahman, J. P. Thomas and K. T. Leung, *Adv. Energy Mater.*, 2018, **8**, 1701234.
42 Z. Bastl, A. I. Senkevich, I. Spirovová and V. Vrtílková, *Surf. Interface Anal.*, 2002, **34**, 477–480.
43 L. Pandolfi, S. Kaciulis, G. Padeletti, A. Cusmà and M. Viticoli, *Surf. Interface Anal.*, 2004, **36**, 1159–1162.
44 L. P. C. Silva, L. E. Terra, A. C. S. L. S. Coutinho and F. B. Passos, *J. Catal.*, 2016, **341**, 1–12.
45 M. K. Dongare, A. M. Dongare, V. B. Tare and E. Kemnitz, *Solid State Ionics*, 2002, **152–153**, 455–462.
46 X. Weng, P. Sun, Y. Long, Q. Meng and Z. Wu, *Environ. Sci. Technol.*, 2017, **51**, 8057–8066.
47 M. R. Goldwasser, M. E. Rivas, E. Pietri, M. J. Pérez-Zurita, M. L. Cubeiro, A. Grivobal-Constant and G. Leclercq, *J. Mol. Catal. A: Chem.*, 2005, **228**, 325–331.
48 R. M. García de la Cruz, H. Falcón, M. A. Peña and J. L. G. Fierro, *Appl. Catal., B*, 2001, **33**, 45–55.
49 J. Ren, X. Liu, R. Gao and W.-L. Dai, *J. Energy Chem.*, 2017, **26**, 681–687.
50 H. Chang, J. Li, X. Chen, L. Ma, S. Yang, J. W. Schwank and J. Hao, *Catal. Commun.*, 2012, **27**, 54–57.
51 Y. Ma, Q. Sun, D. Wu, W.-H. Fan, Y.-L. Zhang and J.-F. Deng, *Appl. Catal., A*, 1998, **171**, 45–55.
52 J. L. G. Fierro, *Catal. Today*, 1990, **8**, 153–174.
53 M. Zhang, M. Dou and Y. Yu, *Phys. Chem. Chem. Phys.*, 2017, **19**, 28917–28927.
54 B. An, J. Zhang, K. Cheng, P. Ji, C. Wang and W. Lin, *J. Am. Chem. Soc.*, 2017, **139**, 3834–3840.
55 J. Ye, C. Liu, D. Mei and Q. Ge, *ACS Catal.*, 2013, **3**, 1296–1306.
56 O. Martin, A. J. Martín, C. Mondelli, S. Mitchell, T. F. Segawa, R. Hauert, C. Drouilly, D. Curulla-Ferré and J. Pérez-Ramírez, *Angew. Chem., Int. Ed.*, 2016, **55**, 6261–6265.

57 M. Fronzi, W. Daly and M. Nolan, *Appl. Catal., A*, 2016, **521**, 240–249.
58 M. A. A. Aziz, A. A. Jalil, S. Triwahyono and S. M. Sidik, *Appl. Catal., A*, 2014, **486**, 115–122.
59 F. Wang, S. He, H. Chen, B. Wang, L. Zheng, M. Wei, D. G. Evans and X. Duan, *J. Am. Chem. Soc.*, 2016, **138**, 6298–6305.
60 C. Morterra, E. Giamello, L. Orio and M. Volante, *J. Phys. Chem.*, 1990, **94**, 3111–3116.
61 D. Bianchi, T. Chafik, M. Khalfallah and S. J. Teichner, *Appl. Catal., A*, 1994, **112**, 219–235.
62 W. Hertl, *Langmuir*, 1989, **5**, 96–100.
63 M. Zhong-Yi, X. Run, Y. Cheng, W. Wei, L. Wen-Huai and S. Yu-Han, *Acta Phys.-Chim. Sin.*, 2004, **20**, 1221–1225.
64 C. Binet and M. Daturi, *Catal. Today*, 2001, **70**, 155–167.
65 K. T. Jung and A. T. Bell, *J. Mol. Catal. A: Chem.*, 2000, **163**, 27–42.
66 T. Akune, Y. Morita, S. Shirakawa, K. Katagiri and K. Inumaru, *Langmuir*, 2018, **34**, 23–29.
67 S. T. Korhonen, M. Calatayud and A. O. I. Krause, *J. Phys. Chem. C*, 2008, **112**, 6469–6476.
68 K. T. Jung and A. T. Bell, *J. Catal.*, 2001, **204**, 339–347.
69 H.-T. Chen and J.-G. Chang, *J. Chem. Phys.*, 2010, **132**, 214702.
70 R. Zhang, M. Peng and B. Wang, *Catal. Sci. Technol.*, 2017, **7**, 1073–1085.
71 K. Samson, M. Śliwa, R. P. Socha, K. Góra-Marek, D. Mucha, D. Rutkowska-Zbik, J. F. Paul, M. Ruggiero-Mikołajczyk, R. Grabowski and J. Słoczyński, *ACS Catal.*, 2014, **4**, 3730–3741.
72 K. Pokrovski, K. T. Jung and A. T. Bell, *Langmuir*, 2001, **17**, 4297–4303.
73 K. T. Jung and A. T. Bell, *Catal. Lett.*, 2002, **80**, 63–68.
74 B. Liu, C. Li, G. Zhang, L. Yan and Z. Li, *New J. Chem.*, 2017, **41**, 12231–12240.